



# Modeling and Analysis of Droplet Evaporation at the Interface of a Coupled Free-Flow–Porous Medium System

Maziar Veyskarami<sup>1</sup> · Carina Bringedal<sup>1,2</sup> · Rainer Helmig<sup>1</sup>

Received: 22 February 2024 / Accepted: 14 August 2024 / Published online: 18 October 2024  
© The Author(s) 2024

## Abstract

Evaporation of droplets formed at the interface of a coupled free-flow–porous medium system enormously affects the exchange of mass, momentum, and energy between the two domains. In this work, we develop a model to describe multiple droplets' evaporation at the interface, in which new sets of coupling conditions including the evaporating droplets are developed to describe the interactions between the free flow and the porous medium. Employing pore-network modeling to describe the porous medium, we take the exchanges occurring on the droplet–pore and droplet–free-flow interfaces into account. In this model, we describe the droplet evaporation as a diffusion-driven process, where vapor from the droplet surface diffuses into the surrounding free flow due to the concentration gradient. To validate the model, we compare the simulation results for the evaporation of a single droplet in a channel with experimental data, demonstrating that our model accurately describes the evaporation process. Then, we examine the impact of free-flow and porous medium properties on droplet evaporation. The results show that, among other factors, velocity and relative humidity in the free-flow domain, as well as pore temperature in the porous medium, play key roles in the droplet evaporation process.

**Keywords** Droplet evaporation · Free-flow–porous medium interface · Coupling · Pore-network model

## 1 Introduction

Formation and evaporation of droplets on the interface of a coupled free-flow-porous medium system appears in natural processes, e.g., human perspiration, where sweat droplets form and evaporate at the surface of our porous skin, and in many engineering applications such as fuel cells, cooling systems, membrane emulsification and filtration,

---

✉ Maziar Veyskarami  
maziar.veyskarami@iws.uni-stuttgart.de

<sup>1</sup> Institute for Modelling Hydraulic and Environmental Systems, University of Stuttgart, Pfaffenwaldring 61, 70569 Stuttgart, Germany

<sup>2</sup> Department of Computer science, Electrical engineering and Mathematical sciences, Western Norway University of Applied Sciences, Inndalsveien 28, 5063 Bergen, Norway

thermal insulation and air-conditioning of buildings (Zhu et al. 2007; Arai and Suidzu 2013; Glass et al. 2001; Charcosset 2009; Rashidi et al. 2018).

Numerous studies have been carried out to investigate droplet evaporation, a few of which we discuss here. Considering the evaporation of a spherical droplet as a stationary process, Maxwell (1890) characterized the evaporation as a diffusion-driven process. Due to variation of the droplet properties, e.g., droplet radius and temperature, referring to the droplet evaporation as a quasi-stationary process is more accurate (Fuchs 1959). Fang et al. (2005) described the droplet evaporation into free flow (air) as consisting of two parts: the diffusion part, which is diffusion of the vapor into the air and is controlled by the diffusion coefficient, and the evaporation part, which is the flow of the liquid molecules inside the droplet to its surface and is regulated by the latent heat of vaporization.

Evaporation of droplets at the interface of a coupled free-flow–porous medium system is controlled by various parameters affecting droplet–free-flow, droplet–pore and droplet–solid interactions (Fuchs 1959; Kulinich and Farzaneh 2009; Song et al. 2011; Erbil 2012; Picknett and Bexon 1977). The droplet–free-flow interactions occur through the droplet surface and affect, for instance, diffusion of vapor from the surface of the droplet into the free flow (Fang et al. 2005). The droplet–pore interactions determine energy and mass exchange between the droplet and the connected pore body. The mode of droplet evaporation, triple contact line dynamics and contact angle changes are dependent on the droplet–solid surface interactions. Compared to a liquid droplet fully surrounded by a gas phase, the evaporation of a sessile droplet in a gas phase is slower due to the presence of the solid substrate, which hinders evaporation (Picknett and Bexon 1977).

For an evaporating droplet on a solid surface, two pure modes of evaporation are recognized: Constant contact angle mode and constant contact radius mode (Picknett and Bexon 1977). The evaporation process can occur as a combination of these two modes, depending on the surface properties and free-flow conditions (Bourges-Monnier and Shanahan 1995). Stick–slip motion of the evaporating droplet is observed on surfaces with low pinning ability, whereas surfaces with high pinning ability exhibit high contact angle hysteresis (Bormashenko et al. 2011). Experimental findings also demonstrate that on surfaces with more hydrophobicity, the contact line depins more easily during the evaporation (Orejon et al. 2011; Shin et al. 2009). Kulinich and Farzaneh (2009) showed that the pinning ability of the surface determines the evaporation mode of a droplet on a super-hydrophobic surface with a contact angle larger than  $150^\circ$ . They observed that on a surface with a high pinning ability, i.e., high contact angle hysteresis of the droplet on the surface, the contact area of the droplet remains nearly constant during evaporation, while the contact angle steadily decreases. However, a droplet on a surface with low pinning ability, i.e., low contact angle hysteresis of the droplet on the surface, follows mostly a constant contact angle and a decreasing contact area mode. Their results indicate that evaporation of a droplet on a surface with high pinning ability occurs more rapidly.

To investigate the impact of surface properties on the evaporation of sessile droplets, Sobac and Brutin (2011) conducted experiments using nano- and micro-coatings to vary surface roughness and wettability. They found that the impact of the contact angle on evaporation is more significant when the contact angle is greater. Investigating droplet evaporation on hydrophobic surfaces with small contact angle hysteresis, Dash and Garimella (2013) found a good agreement between experimental data and a diffusion-only model for a case of smooth hydrophobic surfaces. However, for super-hydrophobic solid surfaces with low contact angle hysteresis, the model overpredicted the evaporation rate (Dash and Garimella 2013).

How another evaporating droplet affect the evaporation of a droplet on a hydrophobic surface was analyzed by Shaikeea and Basu (2016). They found that depending on the distance between the droplets, the evaporation rate of a pair of droplets could be less than or equal to that of a single droplet. They also observed an asymmetric shrinkage of the droplets due to evaporation as a result of the presence of the other droplet. The interactions between multiple evaporating droplets was also investigated by Hatte et al. (2019). They analyzed the influence of the contact angle, the distance between the droplets, and spatial arrangement of droplets, i.e., if a droplet is positioned between others or adjacent to a single droplet, on the evaporation process. They presented a theoretical model to predict the evaporation of multiple droplets. Their findings indicate that vapor accumulation around the droplets induces asymmetric evaporation flux from their surfaces and also increases the droplet evaporation time.

In a case where a droplet is in a channel, the confinement affects the evaporation process. This impact was studied by Bansal et al. (2017). Their findings reveal that compared to unconfined droplets, confinement in a channel extends the overall evaporation time of the droplet due to accumulation of the water vapor within the channel.

In Veyskarami et al. (2023), we discussed droplet formation and detachment at the interface between a free flow and a porous medium. In the current work, we focus on the modeling of droplet evaporation and the impact of free-flow and porous medium parameters on this process. The aim of the present study is to develop a model being able to handle the formation and evaporation of multiple droplets at the interface between a free flow and a porous medium. Since interface processes dominate the overall behavior of such a coupled system, we also focus on deriving the coupling conditions applying to mass and energy transport between the two flow domains through the interface and in the presence of droplets. Similar to Veyskarami et al. (2023), we use pore-network modeling to describe the porous medium. We simulate evaporation of a sessile droplet in a channel and compare the simulation results with experimental data. Then, we analyze how free-flow conditions, such as free-flow velocity and relative humidity, and porous medium conditions, such as contact angle and pore temperature, affect the droplet evaporation.

The paper is structured as follows: In Sect. 2, first, we explain the models that are used to describe each domain, followed by description of interactions at the interface and development of proper coupling conditions including droplet impact. In the last part of this section, we focus on droplet evaporation. In Sect. 3, we present a comparison between numerical results and experimental data for droplet evaporation in a channel. After that, we analyze the impact of free-flow and porous medium properties on droplet evaporation. Then, we finish Sect. 3 by presenting an example of evaporation of multiple droplets at the interface between a free flow and a porous medium, described by a pore network. Finally, we give a summary and outlook in Sect. 4.

## 2 Model Description

In this section, we first describe the model and assumptions that we use to describe the porous medium through pore-network modeling. Then, the model used to describe the free-flow domain is presented. Subsequently, we discuss the droplet description and interactions at the interface between the domains, followed by deriving a coupling concept that includes the droplet impacts. The final part focuses on droplet evaporation. It should be noted that a few parts of the current section have already been discussed in

detail in our previous paper (Veyskarami et al. 2023), which focused on droplet formation and detachment at the interface. Since they are also relevant for the present work with the focus on the droplet evaporation, we mention them here as well.

## 2.1 Porous Medium

We use pore-network modeling to describe the porous medium. A pore-network model approximates the porous medium as a network of large void spaces called pore bodies, which are connected by narrow void spaces known as pore throats in a solid bulk. Figure 1 shows two pore bodies,  $i$  and  $j$ , connected to each other by pore throat  $ij$ . In a pore-network model, the primary variables are located at the center of bodies, where the balance equations need to be fulfilled and pore throats determine the flow conductivity (Blunt 2017).

### Mass balance

In a multiphase compositional system, Eq. (1) describes the mass balance for each component  $\kappa$  on each pore body  $i$ :

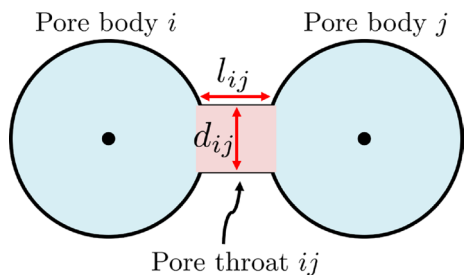
$$V_i \frac{\partial \left( \sum_{\alpha} x_{\alpha}^{\kappa} \rho_{\text{mole},\alpha} S_{\alpha} \right)}{\partial t} + \sum_{\alpha} \sum_j (x_{\alpha}^{\kappa} \rho_{\text{mole},\alpha} Q_{\alpha})_{ij} + \sum_{\alpha} \sum_j \left( j_{\text{diff, mole},\alpha}^{\kappa, \text{pnm}} A_{\alpha} \right)_{ij} = (Vq^{\kappa})_i. \quad (1)$$

In the above equation,  $V_i$  is the volume of pore body  $i$ ,  $x_{\alpha}^{\kappa}$  is the mole fraction of component  $\kappa$  in phase  $\alpha$ ,  $\rho_{\text{mole},\alpha}$  is the molar density of phase  $\alpha$ ,  $S_{\alpha}$  indicates the saturation of phase  $\alpha$ ,  $Q_{\alpha,ij}$  is the flow rate of phase  $\alpha$  in pore throat  $ij$ ,  $j_{\text{diff, mole},\alpha}^{\kappa, \text{pnm}}$  is the diffusive flux of component  $\kappa$  in each phase  $\alpha$  through each pore throat  $ij$ ,  $A_{\alpha}$  is the cross-sectional area of phase  $\alpha$  in the pore throat, and  $q^{\kappa}$  is the possible source or sink term. The Fick's first law describes  $j_{\text{diff, mole}}^{\kappa, \text{pnm}}$  as:

$$j_{\text{diff, mole},\alpha,ij}^{\kappa, \text{pnm}} = -\frac{1}{M^{\kappa}} \frac{\rho_{\alpha,j} + \rho_{\alpha,i}}{2} \frac{D_{\alpha,j}^{\kappa} + D_{\alpha,i}^{\kappa}}{2} \frac{X_{\alpha,j}^{\kappa} - X_{\alpha,i}^{\kappa}}{l_{ij}}, \quad (2)$$

where  $M^{\kappa}$  is molar mass of component  $\kappa$ ,  $\rho_{\alpha}$  is density of phase  $\alpha$ ,  $D_{\alpha}^{\kappa}$  is the binary diffusion coefficient of component  $\kappa$  in phase  $\alpha$ , which is a function of pressure and temperature

**Fig. 1** Pore throat  $ij$  connects pore bodies  $i$  and  $j$  (Veyskarami et al. 2023)



in each pore body,  $X$  is the mass fraction of component  $\kappa$  and  $l_{ij}$  is the length of the pore throat connecting the two pore bodies.

### Momentum equation

Neglecting the impact of gravity, the general equation to calculate the flow rate of phase  $\alpha$ ,  $Q_{\alpha,ij}$ , in pore throat  $ij$  connecting pore bodies  $i$  and  $j$  is:

$$Q_{\alpha,ij} = -g_{\alpha,ij}(p_{\alpha,j} - p_{\alpha,i} + \Psi_{\alpha}), \quad (3)$$

where the throat conductance,  $g_{\alpha}$ , can be calculated as a function of the effective cross-sectional area and the effective radius related to the phase  $\alpha$  in the throat. A detailed description of different approaches to calculate  $g_{\alpha}$  is given by, e.g., Weishaupt (2020) and Wu et al. (2023).  $p_{\alpha}$  is the pressure of each phase and  $\Psi_{\alpha} = \rho_{\alpha} \mathbf{g}(\mathbf{X}_j - \mathbf{X}_i)$  is the influence of gravity, where  $\mathbf{g}$  is the gravity vector and  $(\mathbf{X}_j - \mathbf{X}_i)$  is the distance vector between the centers of pore bodies  $i$  and  $j$ .

### Energy balance

The energy balance in each pore body,  $i$ , can be written as:

$$\begin{aligned} V_i \frac{\partial \left( \sum_{\alpha} \rho_{\alpha} u_{\alpha} S_{\alpha} \right)}{\partial t} + \sum_{\alpha} \sum_j (\rho_{\alpha} h_{\alpha} Q_{\alpha})_{ij} \\ + \sum_{\alpha} \sum_j (-\lambda_{\alpha} \nabla T A_{\alpha})_{ij} + \sum_{\alpha} \sum_j \left[ A_{\alpha} \sum_{\kappa} \left( j_{\text{diff},\alpha}^{\kappa, \text{pnm}} h_{\alpha}^{\kappa} \right) \right]_{ij} = (V q^e)_i. \end{aligned} \quad (4)$$

Here,  $u$  is the specific internal energy, and  $h_{\alpha}$  is the specific phase enthalpy, which is obtained by:

$$h_{\alpha} = \sum_{\kappa} X_{\alpha}^{\kappa} h_{\alpha}^{\kappa}. \quad (5)$$

Further,  $\lambda_{\alpha}$  is phase heat conductivity and is computed by:

$$\lambda_{\alpha} = \frac{2\lambda_{\alpha,j}\lambda_{\alpha,i}}{\lambda_{\alpha,j} + \lambda_{\alpha,i}}, \quad (6)$$

and  $q^e$  is the possible energy source or sink term.

## 2.2 Free-Flow Domain

### Mass balance

The following balance equation is solved for each component  $\kappa$  in the single-phase multi-component free-flow domain.

$$\frac{\partial x^{\kappa} \rho_{\text{mole}}}{\partial t} + \nabla \cdot \left( x^{\kappa} \rho_{\text{mole}} \mathbf{v} + \mathbf{j}_{\text{diff, mole}}^{\kappa, \text{ff}} \right) = q_{\text{mole}}^{\kappa}. \quad (7)$$

In the above equation,  $\mathbf{v}$  is the velocity vector and the subscript mole indicates that the molar value of the parameter is used in the calculations. The diffusive flux,  $\mathbf{j}_{\text{diff, mole}}^{\kappa, \text{ff}}$ , is approximated by Fick's first law for component  $\kappa$  as:

$$j_{\text{diff, mole}}^{\kappa, \text{ff}} = -\frac{1}{M^\kappa} \rho D^\kappa \nabla X^\kappa, \quad (8)$$

### Momentum balance

The Navier–Stokes equations describe the momentum balance in the free-flow ,

$$\frac{\partial(\rho \mathbf{v})}{\partial t} + \nabla \cdot (\rho \mathbf{v} \otimes \mathbf{v}) + \nabla \cdot (p \mathbf{I} - \mu(\nabla \mathbf{v} + \nabla \mathbf{v}^T)) - \rho \mathbf{g} = 0 \quad (9)$$

where  $p$  is the fluid pressure,  $\mu$  is the fluid viscosity and  $\mathbf{g}$  is the gravity vector.

### Energy balance

For a non-isothermal free flow, we use the following relation to describe the energy balance in the system:

$$\frac{\partial(\rho u)}{\partial t} + \nabla \cdot (h \rho \mathbf{v}) - \nabla \cdot (\lambda \nabla T) + \sum_{\kappa} \nabla \cdot (j_{\text{diff}}^{\kappa, \text{ff}} h^\kappa) = q^e, \quad (10)$$

where  $h$  is the specific phase enthalpy, which in a compositional system can be computed as:

$$h = \sum_{\kappa} X^\kappa h^\kappa. \quad (11)$$

The contribution of diffusive energy transport in a compositional system is described by the fourth term of equation Eq. (10),  $\sum_{\kappa} \nabla \cdot (j_{\text{diff}}^{\kappa, \text{ff}} h^\kappa)$ . The possible energy sink or source term is accounted by  $q^e$ .

### Discretization method

We employ a staggered-grid finite volume approach to discretize the free-flow balance equations in space. In such an approach, the velocity degrees of freedom are located at the faces of the primary cells, which correspond to the centers of the relevant secondary grid cells. The remaining degrees of freedom, such as pressure, temperature, and mole/mass fractions, are located at the centers of the primary grid cells. A detailed description on the staggered-grid finite volume approach is provided by, e.g., Schneider et al. (2020).

## 2.3 Interactions at the Interface

In a coupled system of a free flow and a porous medium without droplets, the two domains interact with each other directly through an interface. However, when droplets form at the interface, they cover a portion of it and influence the interaction between the two flow domains. Figure 2 illustrates a droplet formed at the interface between a pore and the free flow. We need to distinguish between two interfaces:  $\Gamma_{\text{pore}}^{\text{drop}}$  between the pore covered with a droplet and the droplet, and  $\Gamma_{\text{drop}}^{\text{ff}}$  between the droplet formed at the interface and the free flow. These interfaces and their unit normal vectors are shown in Fig. 2.

It should be noted that the models developed in this work are applicable to hydrophobic interfaces and porous media and can be utilized for hydrophilic media with minor adjustments.

In the next parts, we discuss the droplet–pore and droplet–free-flow interactions. Then, we derive the coupling conditions describing the exchange of mass, momentum and energy at the interface, including the droplet impact.

Fig. 2 Interface configuration

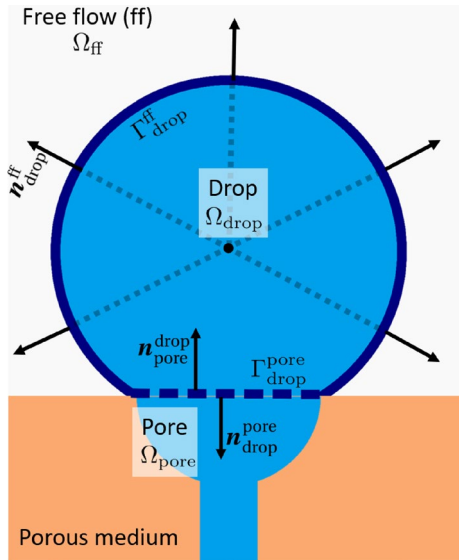
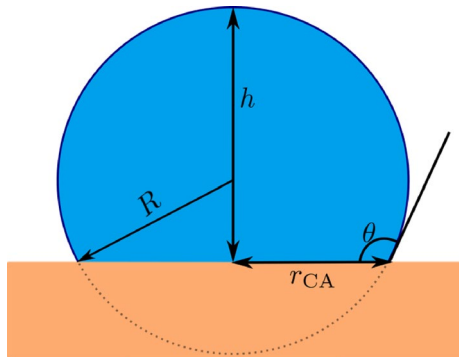


**Fig. 3** Description of a spherical sessile droplet (Veyskarami et al. 2023). Here,  $R$  is the droplet radius of curvature,  $r_{CA}$  is the contact radius of the droplet with the solid surface,  $h$  is the height of the droplet, and  $\theta$  is the droplet contact angle



### 2.3.1 Droplet Geometry

We describe a droplet at the interface as a spherical cap having a circular contact area with the solid surface. Figure 3 illustrates such a droplet and its key descriptive parameters. This assumption holds when the surface is homogeneous and the droplet size is sufficiently small such that the effect of the gravity field is negligible, i.e., Bond number  $\ll 1$  (e.g., Lubarda and Talke 2011). Equations (12) and (13) are used to describe the droplet volume,  $V_{\text{drop}}$ , and the capillary pressure at the droplet surface,  $p_c$ , where  $\gamma_{lg}$  is the surface tension between the phases (e.g., Baber 2014).

$$V_{\text{drop}} = \frac{\pi}{3} h^2 (3R - h) = \frac{\pi}{3} r_{CA}^3 \frac{(1 - \cos(\theta))^2 (2 + \cos(\theta))}{(\sin(\theta))^3}, \quad (12)$$

$$p_c = \frac{2\gamma_{lg}}{R} \frac{2(1 - \cos \theta) + \cos \theta (\sin \theta)^2}{(1 - \cos \theta)^2 (2 + \cos \theta)}. \quad (13)$$

### 2.3.2 Droplet–Porous Medium Interactions

#### Mass balance

A droplet on the surface of the porous medium exchanges mass with the porous medium. Equation (14) shows the mass flux,  $\dot{m}_{\text{drop}}^{\text{pore}}$ , between the droplet and the connected pore through the droplet–pore interface,  $\Gamma_{\text{drop}}^{\text{pore}}$ . In this equation,  $\rho_{\text{pore}}$  is the fluid density in the pore,  $\mathbf{v}_{\text{pore}}^{\text{drop}}$  is the velocity vector of the fluid at  $\Gamma_{\text{drop}}^{\text{pore}}$ , and  $A_{\text{drop}}^{\text{pore}}$  is the area of  $\Gamma_{\text{drop}}^{\text{pore}}$ . The unit normal vector  $\mathbf{n}_{\text{drop}}^{\text{pore}}$  is shown in Fig. 2.

$$\dot{m}_{\text{drop}}^{\text{pore}} = \left[ \rho_{\text{pore}} \mathbf{v}_{\text{pore}}^{\text{drop}} \right] \cdot \mathbf{n}_{\text{drop}}^{\text{pore}} A_{\text{drop}}^{\text{pore}} \text{ at } \Gamma_{\text{drop}}^{\text{pore}}. \quad (14)$$

We assume that the droplet contains the same fluid as the connected pore body, i.e., there is no mole fraction gradient. Consequently, no diffusive mass exchange occurs between the droplet and the connected pore.

It should also be noted that  $\mathbf{v}_{\text{pore}}^{\text{drop}}$  is determined based on the fluid velocity in the pore throat connecting the interface pore body with the neighboring pore body. That means that the fluid exchange between the interface pore body and the neighboring pore bodies directly affects the droplet formed at the interface pore body.

#### Momentum balance

At the interface between a droplet and a pore,  $\Gamma_{\text{drop}}^{\text{pore}}$ , continuity of forces in the normal direction to the droplet surface is described as:

$$\mathbf{F}_{\text{pore}} + \mathbf{F}_{\text{drop}} = 0 \text{ at } \Gamma_{\text{drop}}^{\text{pore}}, \quad (15)$$

where  $\mathbf{F}_{\text{pore}}$  and  $\mathbf{F}_{\text{drop}}$  are the forces exerted on the droplet–pore interface due to the pore body and the droplet pressure, respectively. Veyskarami et al. (2023) showed that under reasonable assumptions, continuing of forces on the droplet–pore interface reduces to:

$$p_{\text{pore}} = p_{\text{drop}} \text{ at } \Gamma_{\text{drop}}^{\text{pore}}, \quad (16)$$

which shows that the pore pressure is equal to the droplet pressure at  $\Gamma_{\text{drop}}^{\text{pore}}$ . We assume no pressure gradient inside the droplet, which leads to equality of the pressure inside the droplet and the pressure at the droplet–pore interface. In the pore-network model, only one pressure is considered for each pore body. According to these assumptions, Eq. (16) not only holds at the interface, but also for the entire droplet and the connected pore,  $\Omega_{\text{drop}} \cup \Omega_{\text{pore}}$ .

#### Energy balance

At  $\Gamma_{\text{drop}}^{\text{pore}}$ , the temperatures of the droplet and the pore are assumed to be equal.

$$T_{\text{drop}} = T_{\text{pore}} \text{ at } \Gamma_{\text{drop}}^{\text{pore}}. \quad (17)$$

Assuming no temperature gradient inside the droplet due to the small size of the droplet, we assign a single temperature value for the entire droplet. Making the same assumption for the pore in pore-network model, the temperature of a pore is described using only one value. Thus, in our model, Eq. (16) is not only valid at the interface, but also for the whole droplet and the pore,  $\Omega_{\text{drop}} \cup \Omega_{\text{pore}}$ . Consequently, energy exchange between the pore and



the droplet,  $\dot{e}_{\text{pore}}^{\text{drop}}$ , occurs only through convection. The convective heat transfer can be expressed by Eq. (18).

$$\dot{e}_{\text{drop}}^{\text{pore}} = \left[ \rho_{\text{pore}} h_{\text{pore}} \mathbf{v}_{\text{pore}}^{\text{drop}} \right] \cdot \mathbf{n}_{\text{drop}}^{\text{pore}} A_{\text{drop}}^{\text{pore}} \text{ at } \Gamma_{\text{drop}}^{\text{pore}}. \quad (18)$$

It is worth mentioning that by considering the same temperature and pressure for the droplet and the pore, the density,  $\rho$ , and the specific enthalpy,  $h$ , of the droplet and the pore are equal as well. Figure 4 illustrates the droplet mass and energy exchange with the connected pore and the surrounding free flow.

### 2.3.3 Droplet–Free-Flow Interactions

#### Mass balance

The part of the free-flow domain that is occupied by the droplet,  $\Omega_{\text{drop}}$ , is treated using a Dirichlet-type condition for mole/mass fraction, i.e., we assign the mole/mass fraction of the droplet for component  $\kappa$  to the cells that are occupied by the droplet:

$$x_{\text{ff}}^{\kappa} = x_{\text{drop}}^{\kappa} \text{ at } \Omega_{\text{drop}}. \quad (20)$$

#### Momentum balance

We have that  $\mathbf{F}_{\text{ff}}$  is the sum of three forces:

$$\mathbf{F}_{\text{ff}} = \mathbf{F}_{\rho v^2} + \mathbf{F}_p + \mathbf{F}_{\tau_{\text{ff}}}. \quad (22)$$

Using the definition of each force provided by Veyskarami et al. (2023), we derive Eq. (23), which shows the mechanical coupling condition at the interface between the droplet and the free flow.

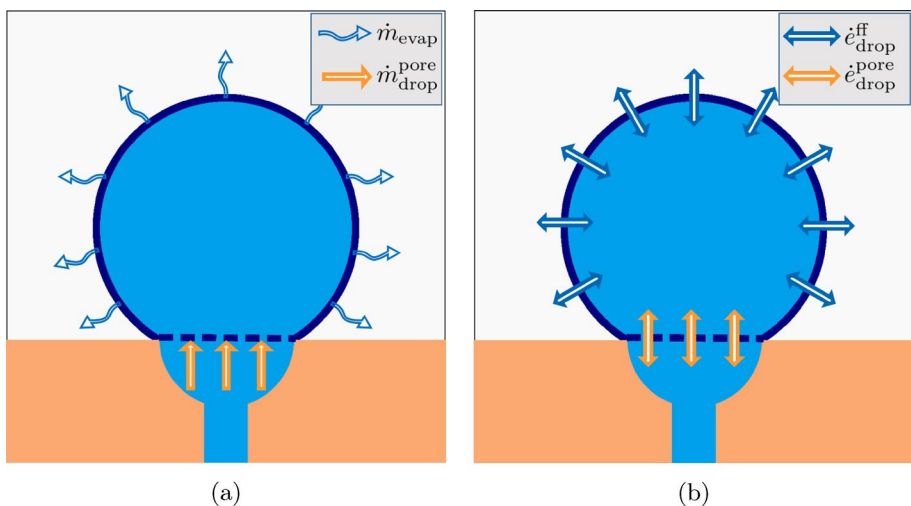


**Fig. 4** **a** Mass exchange between the free-flow, droplet and pore, and **b** Energy exchange between the free-flow, droplet and pore

$$[(\rho \mathbf{v} \otimes \mathbf{v}) + P\mathbf{I} + (-\boldsymbol{\tau}))_{\text{ff}} + P_c \mathbf{I} - p_{\text{drop}} \mathbf{I}] \mathbf{n}_{\text{ff}}^{\text{drop}} \cdot \mathbf{n}_{\text{drop}}^{\text{ff}} da_{\text{drop}}^{\text{ff}} = 0 \text{ at } \Gamma_{\text{drop}}^{\text{ff}}. \quad (23)$$

The part of the free-flow domain which is occupied by the droplet is treated using a Dirichlet-type condition for velocity. As previously mentioned, in the discretized free-flow domain using the staggered-grid finite volume approach, the velocity degrees of freedom are located at the face of grid cells. Thus, we assign zero velocity to the faces which are occupied by the droplet.

$$\mathbf{v}_{\text{ff}} = 0 \text{ at } \Omega_{\text{drop}}. \quad (24)$$

### Energy balance

Energy exchange between the droplet and the free flow takes place at the surface of the droplet through two mechanisms: heat conduction and heat transfer due to the evaporation. Heat conduction occurs as a result of temperature gradient between the surface of the droplet and the surrounding free flow. Additionally, evaporation from the droplet surface causes energy exchange in the form of molecular diffusive energy transfer. By summing the energy transfers through these two mechanisms and integrating over the droplet surface, the total energy exchange between the droplet and the free flow is obtained:

$$\dot{e}_{\text{drop}}^{\text{ff}} = \int_{A_{\text{drop}}^{\text{ff}}} \left[ -\lambda_{\text{ff}} \nabla T_{\text{drop}}^{\text{ff}} + \mathbf{f}_{\text{evap}} h_{\text{drop}}^{\kappa} \right] \cdot \mathbf{n}_{\text{drop}}^{\text{ff}} da \text{ at } \Gamma_{\text{drop}}^{\text{ff}}. \quad (25)$$

Here,  $\lambda_{\text{ff}}$  is the free-flow conductivity,  $\nabla T_{\text{drop}}^{\text{ff}}$  refers to the temperature gradient between the droplet surface and the free flow,  $\mathbf{f}_{\text{evap}}$  is the evaporative flux computed by Eq. (36), and  $h_{\text{drop}}^{\kappa}$  is the specific enthalpy of the main component, e.g.,  $\text{H}_2\text{O}$ , in the droplet.

The droplet temperature is assigned to the part of the free-flow domain that is occupied by the droplet,  $\Omega_{\text{drop}}$ :

$$T_{\text{ff}} = T_{\text{drop}} \text{ at } \Omega_{\text{drop}}. \quad (26)$$

### Droplet impact on the free-flow field

In this section, we explain how the free-flow parts invaded by the droplet are recognized and treated.

To include the impact of the droplet on the free flow, we adopt a simplified approach introduced by Veyskarami et al. (2023). In this approach, we keep the free-flow domain single-phase and the free flow sees the droplet as an obstacle, which might grow or shrink over time. In the discretized free-flow domain, the free-flow cell centers or faces that are occupied by the droplet are recognized. It should be noted that we do not solve for the degrees of freedom inside the droplet; instead, they are treated using Dirichlet-type conditions. In fact, we assign a fixed value to the degrees of freedom located within the droplet region. That means that the free-flow grid cells that are inside the droplet are treated using Eqs. (20) and (26), and the free-flow grid faces that are inside the droplet are treated using Eq. (24). Furthermore, we calculate the temperature and mole/mass fraction gradient between the cells recognized as interface grid cells and the cells inside the droplet. The free-flow shear and inertial forces are evaluated on the interface grid faces, while the pressure force on the interface grid cells. For more details about this approach, we refer to Veyskarami et al. (2023).

### 2.3.4 Coupling Concept for Free Flow and Porous Medium with Droplets

To describe the exchange through the interface between a free flow and a porous medium including droplets' impacts, we need to combine the droplet–pore interactions (see Sect. 2.3.2), and droplet–free-flow interactions (discussed in Sect. 2.3.3).

#### Mass balance

The total mass balance for the droplet in a coupled system can be derived through adding up the droplet mass exchange with the porous medium and the free flow (Veyskarami et al. 2023):

$$\frac{dm_{\text{drop}}}{dt} + \dot{m}_{\text{drop}}^{\text{pore}} + \dot{m}_{\text{drop}}^{\text{ff}} = 0, \quad (27)$$

where

$$\begin{aligned} \frac{dm_{\text{drop}}}{dt} &= \frac{d(\rho_{\text{drop}} V_{\text{drop}})}{dt}, \\ \dot{m}_{\text{drop}}^{\text{pore}} &= [\rho_{\text{pore}} \mathbf{v}_{\text{pore}}^{\text{drop}}] \cdot \mathbf{n}_{\text{drop}}^{\text{pore}} A_{\text{drop}}^{\text{pore}}, \\ \dot{m}_{\text{drop}}^{\text{ff}} &= \dot{m}_{\text{evap}}. \end{aligned} \quad (28)$$

The evaporation from the droplet surface to the free flow is discussed in Sect. 2.4.

As we discussed before, for the parts of the free-flow domain that are occupied by the droplet, we set the mole/mass fractions of the components to the droplet values (Eq. 20).

**Momentum balance** As we do not introduce a new primary variable for the droplet, we formulate the momentum coupling condition for the pore connected to the droplet, including the droplet's effect. Thus, we substitute the droplet pressure in Eq. (23) with the pore pressure according to Eq. (16) which leads to:

$$[(\rho \mathbf{v} \otimes \mathbf{v}) + P\mathbf{I} + (-\boldsymbol{\tau})]_{\text{ff}} + P_c \mathbf{I} - p_{\text{pore}} \mathbf{I} \mathbf{n}_{\text{ff}}^{\text{drop}} \cdot \mathbf{n}_{\text{drop}}^{\text{ff}} da_{\text{drop}}^{\text{ff}} = 0. \quad (29)$$

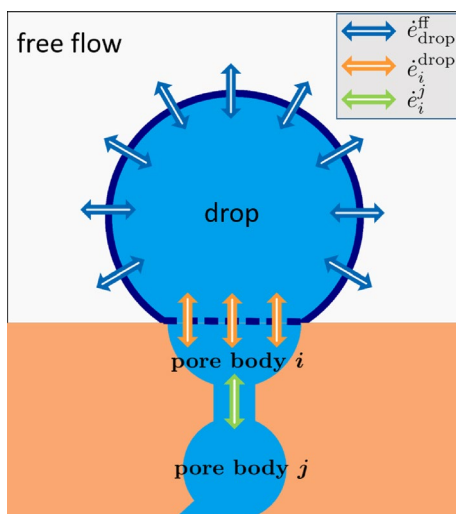
As we discussed before, we assign zero velocity to the parts of the free-flow domain that are occupied by the droplet (Eq. 24).

**Energy balance** Since the droplet temperature is assumed to be equal to the temperature of the interface pore in our model, we write the energy balance for the interface pore and take the pore–free-flow energy exchange through the droplet into account. Considering the configuration shown in Fig. 5 and having no sink/source term, the energy balance for the interface pore body,  $i$ , can be written as:

$$\frac{de_i}{dt} + \dot{e}_i^j + \dot{e}_i^{\text{drop}} + \dot{e}_i^{\text{ff}} = (Vq^e)_i. \quad (30)$$

The first term describes the energy storage in the interface pore body,  $\dot{e}_i^j$  is the energy exchange between the interface pore body  $i$  and the neighboring pore body  $j$ ,  $\dot{e}_i^{\text{drop}}$  is the energy exchange between the interface pore body and the droplet, and  $\dot{e}_i^{\text{ff}}$  is the energy exchange between the interface pore body and the free flow, which occurs through the droplet.

**Fig. 5** Free-flow-droplet-pore energy exchange at the interface



For a case where fluid flows from pore body  $j$  to pore body  $i$  and from pore body  $i$  to the droplet, pore body  $j$  is the upstream pore body for pore body  $i$ , while pore body  $i$  itself is the upwind pore body for the droplet.

We have that  $\dot{e}_i^j$  can be described using the following equation:

$$\dot{e}_i^j = \left[ \rho_j h_j \mathbf{v}_j^i - \lambda_{ji} \nabla T_i^j \right] \cdot \mathbf{n}_i^j A_i^j. \quad (31)$$

To describe the energy exchange between the interface pore body and the free flow through the droplet, we assume that all energy exchanged at the droplet–free-flow interface,  $\dot{e}_{\text{drop}}^{\text{ff}}$ , is evenly distributed throughout the droplet and the interface pore body. Thus, the amount of  $\dot{e}_i^{\text{ff}}$  is a proportion of  $\dot{e}_{\text{drop}}^{\text{ff}}$  that affects pore body  $i$ . Accordingly, the ratio of the pore body volume,  $V_i$ , to the sum of the pore body and droplet volume,  $V_i + V_{\text{drop}}$ , is used to calculate  $\dot{e}_i^{\text{ff}}$ :

$$\dot{e}_i^{\text{ff}} = \left( \frac{V_i}{V_i + V_{\text{drop}}} \right) \dot{e}_{\text{drop}}^{\text{ff}}. \quad (32)$$

Rewriting Eq. (30) using the definition of each term gives the following relation, which describes the energy balance for pore body  $i$  at the interface,

$$\begin{aligned} & \frac{d(\rho_i u_i V_i)}{dt} + \left[ \rho_j h_j \mathbf{v}_j^i - \lambda_{ji} \nabla T_i^j \right] \cdot \mathbf{n}_i^j A_i^j + \rho_i h_i \mathbf{v}_i^{\text{drop}} \cdot \mathbf{n}_i^{\text{drop}} A_i^{\text{drop}} \\ & + \left( \frac{V_i}{V_i + V_{\text{drop}}} \right) \int_{A_{\text{drop}}^{\text{ff}}} \left[ -\lambda_{\text{ff}} \nabla T_{\text{drop}}^{\text{ff}} + \mathbf{f}_{\text{evap}} h_{\text{drop}}^{\kappa} \right] \cdot \mathbf{n}_{\text{drop}}^{\text{ff}} da = (Vq^e)_i. \end{aligned} \quad (33)$$

In the above equation,  $\mathbf{f}_{\text{evap}}$  is the evaporative flux vector. We treat the energy exchange at the interface for the interfacial pore body as a source/sink term. Such a source/sink term is the sum of the droplet–pore convection heat transfer and the proportion of the energy exchange between the droplet and the free flow, which impacts the pore body. Equation

(34) shows the computation of the source/sink term related to the droplet, which affects pore body  $i$  at the interface,  $Q_i^{\text{drop}}$ :

$$Q_i^{\text{drop}} = -\rho_i h_i v_i^{\text{drop}} \cdot \mathbf{n}_i^{\text{drop}} A_i^{\text{drop}} - \left( \frac{V_i}{V_i + V_{\text{drop}}} \right) \int_{A_{\text{drop}}^{\text{ff}}} [-\lambda_{\text{ff}} \nabla T_{\text{drop}}^{\text{ff}} + \mathbf{f}_{\text{evap}} h_{\text{drop}}^{\kappa}] \cdot \mathbf{n}_{\text{drop}}^{\text{ff}} da. \quad (34)$$

Using the source/sink term given by the above equation, the energy balance relation for pore body  $i$ , Eq. (33), can be rewritten as:

$$\frac{d(\rho_i u_i V_i)}{dt} + [\rho_j h_j v_j^i - \lambda_{ji} \nabla T_i^j] \cdot \mathbf{n}_i^j A_i^j = (Vq^e)_i + Q_i^{\text{drop}}. \quad (35)$$

As we discussed before, for the parts of the free-flow domain that are occupied by the droplet, we set the temperature to the droplet temperature (Eq. 26).

## 2.4 Droplet Evaporation

The mass transfer between a droplet and the surrounding free flow occurs through evaporation from the surface of the droplet. We describe the droplet evaporation as a quasi-stationary diffusion-driven process (Fuchs 1959), wherein the diffusion of vapor from the droplet surface to the gaseous free flow governs the evaporation rate. In other words, the vapor concentration gradient between the droplet surface and the surrounding free flow determines the droplet evaporation. Such a process can be described using Fick's first law. Decomposing the evaporative flux,  $\mathbf{f}_{\text{evap}}$ , into its Cartesian components, e.g.,  $i$ - and  $j$ -directions in a two-dimensional setup shown in Fig. 6b, we use the Fick's first law to calculate the diffusive flux in each direction from the surface of the droplet into the neighboring free-flow cell,  $N$ , as shown by Eq. (36) for  $i$ -direction. The flux in  $j$ -direction is calculated analogously.

$$f_{\text{evap},i} = \rho_{\text{g,ff}} D_{\text{g,ff}}^{\kappa} \frac{X_{\text{g,ff,int}}^{\kappa} - X_{\text{g,ff},N}^{\kappa}}{d_i}. \quad (36)$$

In the above equation, subscripts “g” and “ff” emphasize that the evaporation occurs in the gas phase from the surface of the droplet to the surrounding free flow. Consequently, the parameters used to calculate the evaporative flux are related to the free flow, i.e., gas phase. The mass fraction of component  $\kappa$  in the gas phase at the interface grid face and in the neighboring cell are, respectively, denoted by  $X_{\text{g,ff,int}}^{\kappa}$  and  $X_{\text{g,ff},N}^{\kappa}$ , and  $d_i$  is the distance between the interface grid face and the center of the neighboring grid cell in  $i$ -direction (see Fig. 6b). It should also be noted that the subscripts “int” and “N” indicate the values at the interface grid face and neighboring cell, respectively. Here, the interface grid face is the face of the grid cell that is occupied by the droplet and has a neighboring cell that is outside the droplet.

Integrating the evaporative flux over the surface of the droplet yields the total mass flux leaving the droplet surface due to evaporation,  $\dot{m}_{\text{evap}}$ .

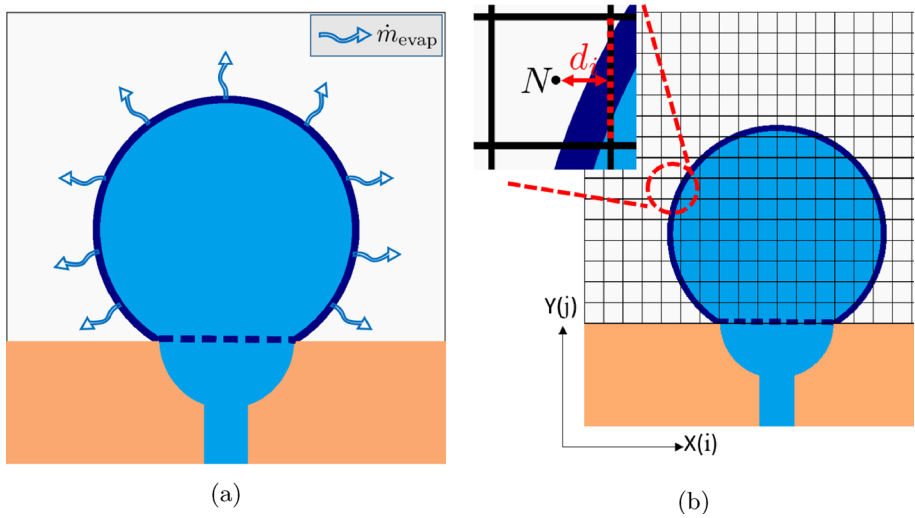


**Fig. 6** **a** Evaporation from the surface of a droplet into the free flow, and **b** an interface grid face (red dashed line) and its neighboring grid cell ( $N$ )

$$\dot{m}_{\text{evap}} = \int_{A_{\text{drop}}^{\text{ff}}} f_{\text{evap}} \cdot \mathbf{n}_{\text{drop}}^{\text{ff}} da. \quad (37)$$

In the above equation, we use  $\mathbf{n}_{\text{drop}}^{\text{ff}}$  to get the evaporative flux from the surface of the droplet in radial direction.

To compute the evaporative flux using Eq. (36), we need the value of  $X_{\text{g,ff,int}}^{\kappa}$  beforehand. To obtain that, we assume mechanical, thermal and chemical equilibrium at the surface of the droplet,  $\Gamma_{\text{drop}}^{\text{ff}}$ . Such equilibrium conditions are demonstrated in Fig. 7.

The mechanical equilibrium at the droplet surface means that the droplet pressure at  $\Gamma_{\text{drop}}^{\text{ff}}$  is equal to the sum of free-flow pressure and capillary pressure. The thermal equilibrium indicates that the temperature of the droplet and the free flow are the same at the droplet surface. According to the chemical equilibrium, a component in the liquid phase (droplet) and the gas phase (free flow) must have the same chemical potential,  $\mu^{\kappa}$ , at the droplet surface.

Having chemical equilibrium at  $\Gamma_{\text{drop}}^{\text{ff}}$ , for the vapor component,  $\kappa$ , Raoult's law can be applied to compute the partial pressure of that component in the gas phase using the vapor pressure,  $p_{\text{vap}}^{\kappa}$ , and the mole fraction of the component  $\kappa$  in the liquid phase,  $x_{\text{l,drop}}^{\kappa}$ :

$$p_{\text{g,ff}}^{\kappa} = p_{\text{vap}}^{\kappa} x_{\text{l,drop}}^{\kappa} \text{ at } \Gamma_{\text{drop}}^{\text{ff}}. \quad (38)$$

Then, using the Dalton's law, the mole fraction of the component  $\kappa$  in the gas phase,  $x_{\text{g,ff}}^{\kappa}$ , at  $\Gamma_{\text{drop}}^{\text{ff}}$  is computed as the ratio of the partial pressure of the component  $\kappa$  to the total gas pressure,  $p_{\text{g,ff}}$ :

$$x_{\text{g,ff}}^{\kappa} = \frac{p_{\text{g,ff}}^{\kappa}}{p_{\text{g,ff}}} \text{ at } \Gamma_{\text{drop}}^{\text{ff}}. \quad (39)$$

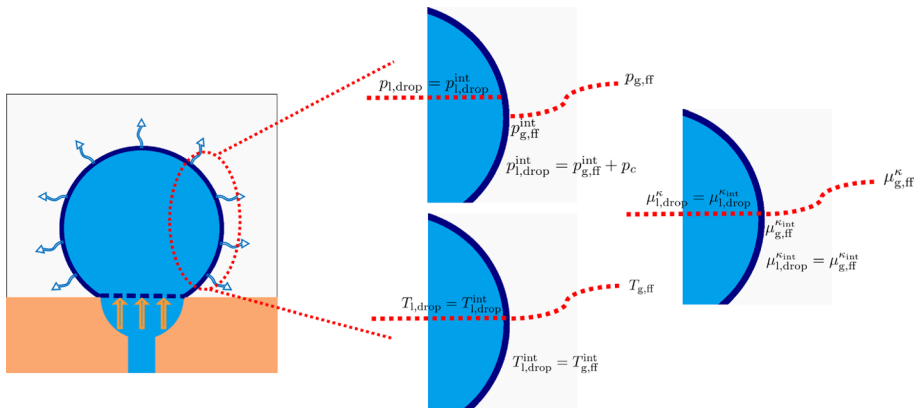


**Fig. 7** Equilibrium conditions at the surface of the droplet

Converting mole fraction to mass fraction is straightforward. We assign the value computed by Eq. (39) to the cells occupied by the droplet. To identify the grid cells in the free-flow domain that are affected by the droplet, we take the approach explained in Sect. 2.3.3. In this study, it is assumed that the mole fraction of the main component in the liquid phase is equal to one.

### Evaporation mode

In our model, the droplet evaporation mode might follow the constant contact area mode or a combination of constant contact angle and constant contact area modes. If the droplet contact radius is equal to the pore body radius, the droplet shrinkage due to the evaporation occurs in a constant contact area mode. In this mode, the contact angle,  $\theta$  of the droplet diminishes during the evaporation, while the droplet contact area remains constant. Shrinkage of a droplet with an initial contact radius greater than the pore radius, however, starts with a constant contact angle mode. The droplet contact radius decreases as long as it is greater than the pore radius, whereas the droplet contact angle remains constant and equal to the surface contact angle,  $\theta_{eq}$ . By further shrinkage of the droplet and when the droplet contact radius reduces to the pore radius, the droplet contact angle begins to decrease and the contact radius stays constant. Such a process is illustrated in Fig. 8.

## 3 Results and Discussion

In this section, we first use the developed model to simulate the evaporation of a single droplet formed at the interface between a free flow and a porous medium in a channel and compare the numerical results with experimental data provided by Bansal et al. (2017). Then, we analyze the impact of free-flow and porous medium properties on the droplet evaporation. At the end, we present a showcase of using our model to simulate evaporation of multiple droplets at the interface between a free flow and a porous medium. All the models developed in this study are implemented in DuMu<sup>x</sup>, an open-source simulation toolbox for transport in porous media (Koch et al. 2021).

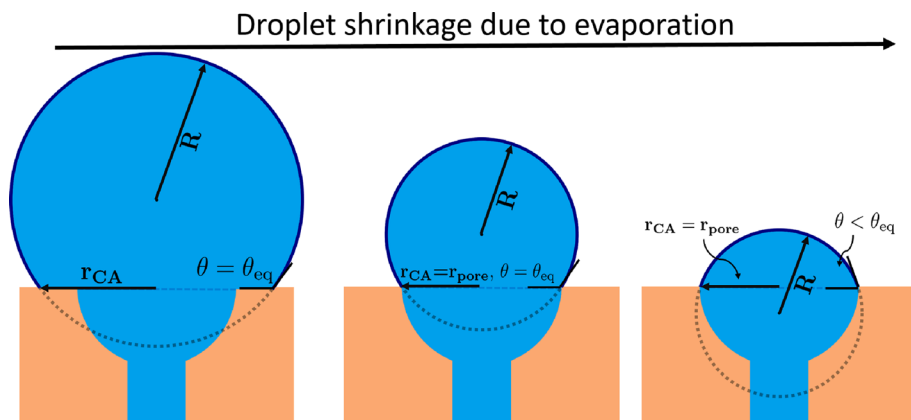


Fig. 8 Droplet evaporation modes

### 3.1 Droplet Evaporation: Comparison with Experimental Data

Bansal et al. (2017) examined the impact of confinement on the evaporation of a sessile droplet. Their results show that evaporation time increases in a channel due to accumulation of vapor around the droplet. The impact of vapor accumulation becomes more significant by increasing the channel length. Bansal et al. (2017) characterized this effect by introducing a vapor accumulation length scale, which determines how far from the droplet the vapor concentration reduces to the ambient concentration.

First, we describe the simulation setup used for the comparison. Then, we present the comparison of simulation and experimental results for evaporation of a single sessile droplet in a channel.

#### 3.1.1 Simulation Setup

The setup used in the experiment is thoroughly discussed in Bansal et al. (2017). Thus, we only focus on the simulation setup in this part. The simulation setup consists of a two-dimensional channel with the height of  $1.2 \times 10^{-3}$  m. The channel length,  $L$ , varies from  $2.55 \times 10^{-3}$  m to  $1.765 \times 10^{-2}$  m. It should be noted that the channel length used here is determined based on the vapor accumulation length scale introduced by Bansal et al. (2017), which is a length that the vapor concentration varies from the concentration at the droplet surface to the ambient concentration. We apply pressure of 1 atm, temperature of 298.15 K, and relative humidity of 45% to the channel inlet and outlet (see Fig. 9). Using a pore connected to the bottom wall of the channel, a droplet with the volume of  $1.5 \times 10^{-9}$  m<sup>3</sup> is formed and then evaporates until it disappears.

#### 3.1.2 Results

Figure 10 shows the impact of channel length on the evaporation time and compares the simulation results and experimental data provided by Bansal et al. (2017) for a single droplet evaporating in a channel. According to the results, there is a good match between the



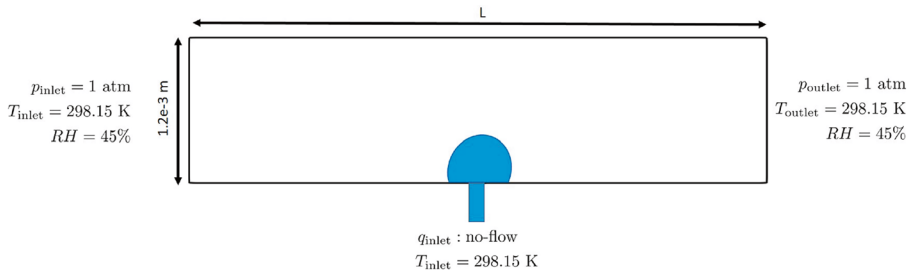
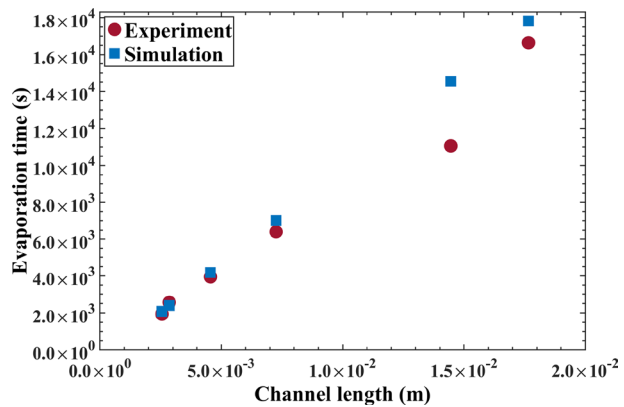


**Fig. 9** Simulation setup and boundary conditions used in comparison with experimental data for droplet evaporation. “L” is the channel length, which varies in each simulation to examine the impact of channel length on droplet evaporation

**Fig. 10** Comparison of simulation results with the experimental data given in Bansal et al. (2017) for impact of channel length on the evaporation of a single droplet confined in a channel



simulation and experimental data and our model is able to predict the impact of the channel length on the evaporation time of the droplet.

Having validated our concept for droplet evaporation using experimental data, we employ our model for analysis for droplet evaporation in the next section.

### 3.2 Droplet Evaporation Analysis

In this section, we analyze the impact of free-flow and porous medium properties on the droplet evaporation at the interface.

#### 3.2.1 Simulation Setup

To simulate a single droplet evaporation, we use a setup shown in Fig. 11. The setup is composed of a two-dimensional free-flow channel and a simple porous medium, which consists of two pore bodies connected by a pore throat.

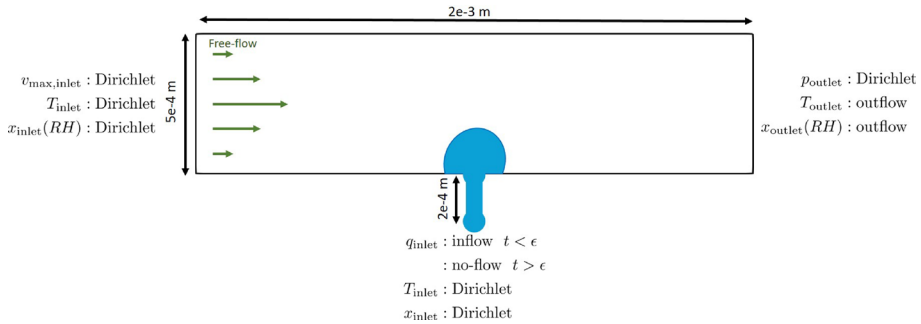


**Fig. 11** The simulation setup used for droplet evaporation analysis: Dimensions and boundary conditions

Initially, the channel is fully filled with gas (air). At the inlet, gas flows into the channel with a fully developed laminar velocity profile. Dirichlet boundary conditions are applied at the inlet for gas velocity, temperature, and mole fraction (relative humidity). At the outlet of the channel, a constant pressure is applied, and outflow boundary conditions are used for temperature and mole fraction.

The porous medium is initially fully saturated with water. At the inlet pore body, Dirichlet boundary conditions are applied for temperature and mole fraction of the components. Water is injected to the inlet pore for a short time,  $\epsilon$ , such that a droplet with an intended volume is formed at the bottom wall of the channel. Then, the injection stops and the droplet starts to shrink due to evaporation until it vanishes from the surface. It should be noted that in comparison with the whole time of the evaporation process, the injection time is so small that droplet evaporation during injection is negligible.

### 3.2.2 Impact of Pore Body Radius (Evaporation Mode)

The two main modes of droplet evaporation are the constant contact angle (CCA) and constant contact radius (CCR). In this section, we analyze the impact of these evaporation modes on droplet evaporation. As the pore body radius is a factor that determines the transition between droplet evaporation modes, using different pore radii alters the duration of each evaporation mode. For a droplet with a given volume, a small pore body connected to the droplet results in the evaporation process predominantly following the CCA mode. This occurs because the evaporation of a droplet with an initial contact radius greater than the pore body radius begins in the CCA mode. The evaporation mode switches to the CCR mode once the contact radius of the droplet decreases to the pore body radius. Therefore, the smaller the pore body radius, the later the switch of evaporation mode occurs. On the contrary, a larger pore body radius results in the CCR mode dominating the evaporation process. In our analysis, we use two different radii for the pore connected to the evaporative droplet: a radius of  $1 \times 10^{-4} \text{ m}$  and another radius of  $5 \times 10^{-5} \text{ m}$ . Figure 12 depicts the modes of evaporation for the two pore body radii in terms of the contact angle and contact radius variation, as well as the change in the volume of the droplets in the two cases. In this figure, the mode of evaporation is indicated using CCA or CCR mode.

Figure 13a shows that the evaporation occurs slightly faster when the pore body radius is smaller, i.e., when the CCA mode dominates the evaporation process. Conversely, when

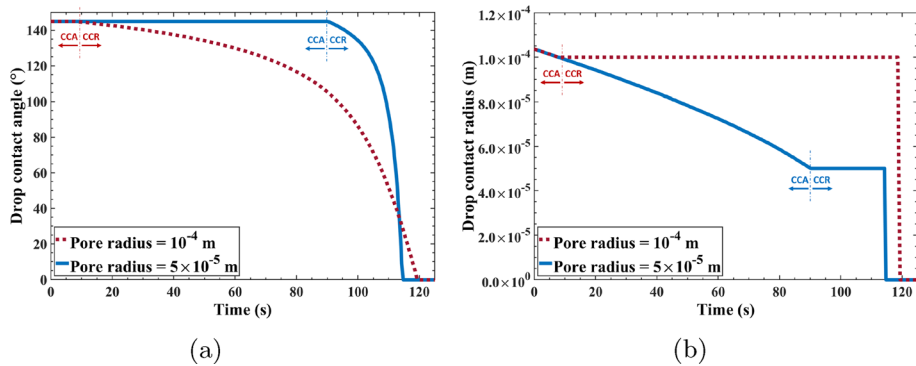


**Fig. 12** Variation of **a** droplet contact angle and **b** droplet contact radius over time during droplet evaporation for two pore body radii

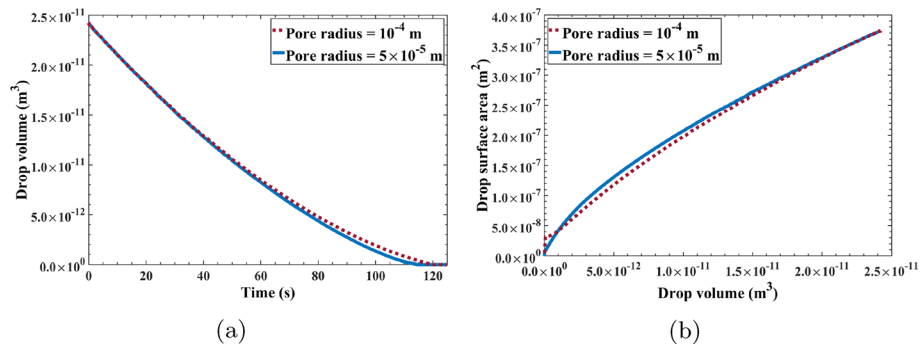


**Fig. 13** Variation of **a** droplet volume over time, and **b** droplet surface area versus droplet volume during droplet evaporation for two pore body radii

the CCR mode is dominant, the droplet's contact angle begins to decrease earlier, leading to a reduction in the droplet's surface area. This results in a slightly slower evaporation process for the CCR mode. This effect can be seen in Fig. 13b, where the change of droplet surface area versus the droplet volume for each evaporation mode is shown.

### 3.2.3 Impact of Free-Flow Relative Humidity

Since the evaporation from the surface of the droplet is diffusion-driven, the relative humidity of the free flow is one of the key parameters affecting the evaporation rate. Figure 14 shows how relative humidity of the free flow influences the droplet evaporation. It should be noted that the inlet free-flow velocity and inlet free-flow temperature, under which these analyses are conducted, are 5 m/s and 298.15 K, respectively. In Fig. 14a, the average evaporation rate versus the relative humidity (RH), which is applied to the inlet of the free-flow channel as a boundary condition, and the pore body temperature is depicted. The average evaporation rate is calculated by dividing the initial droplet mass to the total time of the droplet evaporation, which is the duration required for a droplet to completely evaporate. As expected, increasing the relative humidity of the free flow decreases the

average evaporation rate. The results show that the average evaporation rate decreases almost linearly with the relative humidity for each free-flow temperature. Figure 14b shows the evaporation rate over time for different relative humidities for a case that the pore body temperature is 298.15 K. The evaporation rate reported in this figure is the rate of change in droplet mass due to evaporation. For all cases, the evaporation rate exhibits a downward trend over time, which could be due to the shrinkage of the droplets with time, leading to a reduction in the evaporation rate. The change in the evaporation rate varies throughout the life of the droplet. Each curve experiences a major increase in slope as it approaches its endpoint, which corresponds to the switch in the evaporation from constant contact angle to constant contact radius mode. Following this transition, the evaporation rate decreases more rapidly than before, indicating a slower evaporation process. Furthermore, as a droplet shrinks, its surface moves closer to the bottom wall of the free-flow channel. Consequently, the local velocity of the free flow surrounding the droplet decreases, resulting in a further reduction of the evaporation rate. The impact of the free-flow velocity on the droplet evaporation is examined in Sect. 3.2.5. Figure 14c shows variation of the droplet volume due to the evaporation over time for three different values of relative humidity. This figure is for a case where the pore body temperature is 298.15 K.

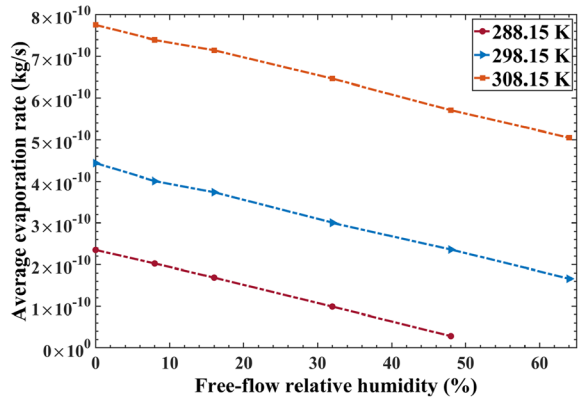
### 3.2.4 Impact of Free-Flow Temperature

Figure 15 shows the change of droplet volume due to evaporation under various inlet free-flow temperatures and relative humidities. It is important to note that the inlet pore body temperature and the inlet free-flow velocity are the same for all cases and are set to 298.15 K and 5 m/s, respectively. According to Fig. 15a, which shows the results for a setup with an inlet relative humidity of 0%, the free-flow temperature has no impact on the droplet evaporation. Two reasons could be given for such a behavior. The first reason could be uniform energy distribution over the droplet and the connected pore body in our model, i.e., no temperature gradient exists inside the droplet or between the droplet and the connected pore body, implying no conductive heat transfer between them. In our model, the free-flow temperature primarily affects the energy exchange between the droplet and the surrounding gas through heat conduction. Given our assumption of no temperature gradient within the droplet and its connected pore body, the energy exchanged with the free flow is consumed to change the temperature throughout the entire droplet and pore body, rather than being concentrated near the droplet surface. Consequently, our model underestimates the change in the droplet surface temperature resulting from energy exchange with the free flow. Another reason is the heat conductive exchange between the interface pore connected to the droplet and the inlet pore body, where a constant temperature of 298.15 K is applied.

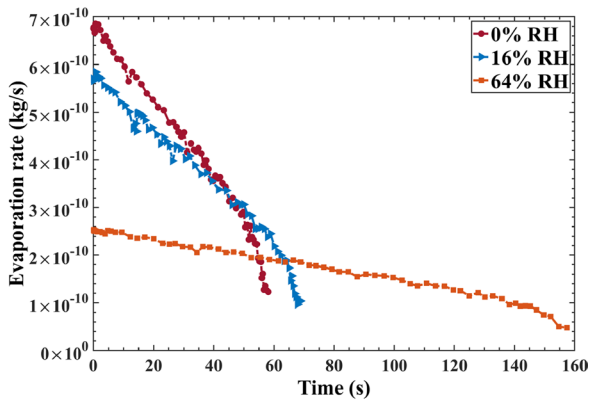
Figure 15b shows that when the inlet relative humidity of the free flow is 16%, increasing the free-flow temperature leads to longer evaporation time. This is because at higher temperatures, a gas phase with a specific relative humidity contains higher vapor concentration. As a result, as temperature increases while relative humidity remains constant, the evaporation rate decreases.

In Fig. 15c, when gas with temperature of 308.15 K and relative humidity of 64% is injected to the inlet of the free-flow channel, droplet evaporation ceases and the droplet volume remains constant. This phenomenon occurs because the cooling effect of the droplet causes the free-flow temperature to approach the dew point in the vicinity of the droplet surface, which stops the evaporation. Although, condensation might be expected

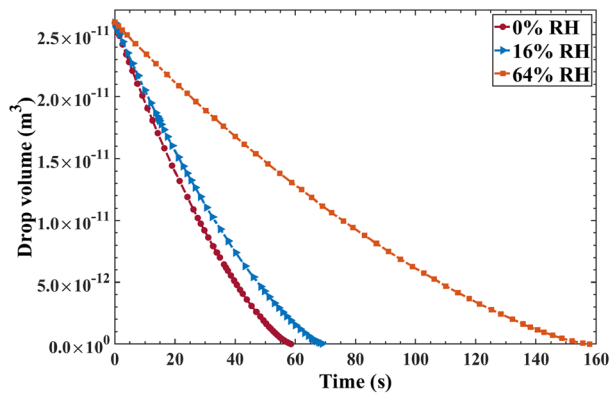
**Fig. 14** Impact of free-flow relative humidity on droplet evaporation: **a** average evaporation rate, **b** evaporation rate for a case where the pore and free-flow inlet temperature are 298.15 K and **c** droplet volume variation over time for a case where the pore and free-flow inlet temperature are 298.15 K



(a)

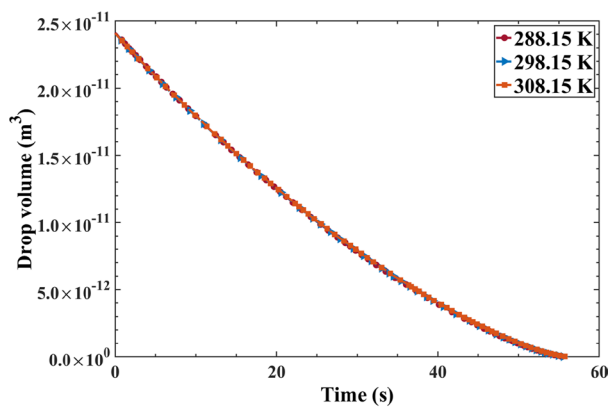


(b)

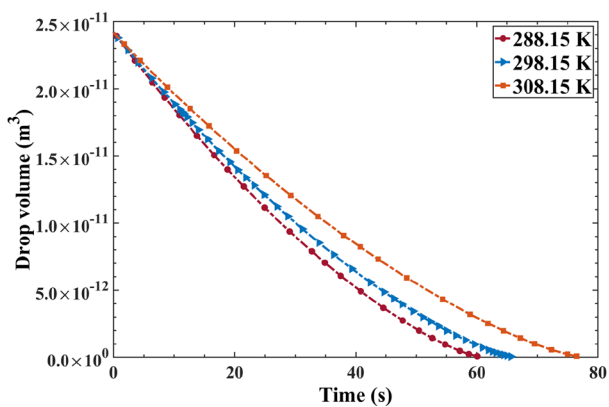


(c)

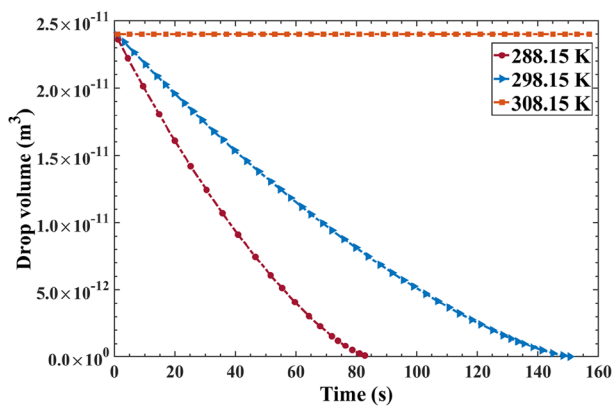
**Fig. 15** Variation of the droplet volume over time due to evaporation in three free-flow temperatures: **a** inlet relative humidity = 0%, **b** inlet relative humidity = 16%, and **c** inlet relative humidity = 64%



(a)



(b)



(c)

under these conditions, since a concept to describe the possible condensation process is not included in our model, the droplet volume remains constant in the simulation.

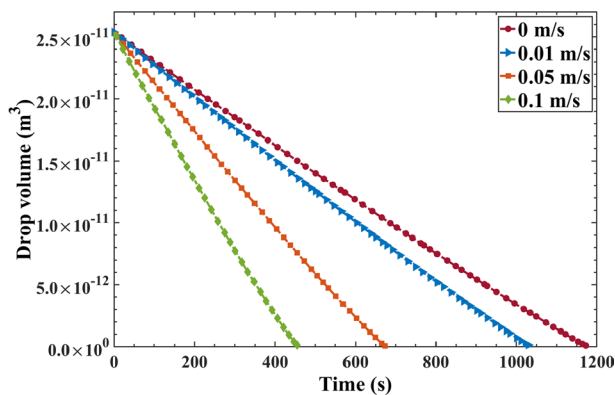
### 3.2.5 Impact of Free-Flow Velocity

To analyze the impact of free-flow velocity on droplet evaporation, we define two velocity ranges: low range (0–0.1 m/s) and high range (0.5–10 m/s). Figure 16 shows how free-flow velocity affects droplet evaporation. The results presented in these figures correspond to cases where both the inlet free-flow and pore temperatures are 298.15 K and the relative humidity of the gas entering the free-flow channel is 16%. Figure 16a and b shows the change in the droplet volume over time due to evaporation for the two ranges of free-flow velocities. The velocity values reported in these figures are the maximum velocities applied at the inlet of the free-flow channel, which occurs on the center line of the channel. Figure 16a, which presents results for the low range of free-flow velocities, demonstrates that the droplet volume decreases at an almost constant rate throughout the entire period, indicating a quite constant evaporation rate over time. For the high range of free-flow velocities shown in Fig. 16b, however, the rate of the droplet shrinkage declines over time, i.e., decreasing the evaporation rate with time. Such a behavior becomes more evident in Fig. 16c, showing the evaporation rate over time shown, where the droplet evaporation rate experiences a rapid decrease over time when the free-flow velocity is 0.5 m/s compared to the more gradual changes observed at lower velocities. Considering the velocity profile in the channel, the velocity varies from zero at the walls to its maximum at the centerline of the channel. As the droplet shrinks due to the evaporation, its surface moves further from the center line and closer to the bottom wall. In fact, the effective free-flow velocity acting on the droplet surface decreases as the droplet shrinks, which accelerates the reduction of the evaporation rate. This change in the velocity of the free flow impacting the droplet becomes more considerable at higher free-flow velocities.

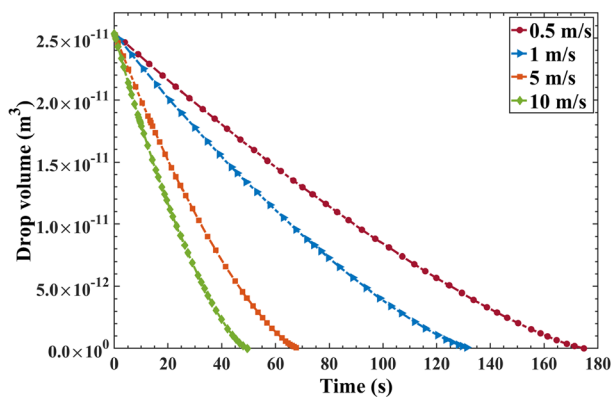
How the impact of free-flow velocity on evaporation differs with the relative humidity of free flow is shown in Fig. 17. As Fig. 17a shows, increasing the free-flow velocity promotes droplet evaporation across all relative humidity levels, with the effect being more pronounced at lower initial velocities. Moreover, the influence of free-flow velocity on the evaporation rate is more significant when the relative humidity of the gas entering the free-flow channel is lower. Such a behavior is also reflected in the variation of average evaporation rate with Peclet number shown in Fig. 17b. The Peclet number used here is defined as  $Pe = v\Delta y/D$ , where  $v$  is the maximum velocity applied to the inlet of the free-flow channel,  $\Delta y$  is the grid-cell length normal to the flow direction and  $D$  is the binary diffusion coefficient.

According to our assumptions, local thermodynamic equilibrium holds at the surface of the droplet. This implies that the air immediately adjacent to the droplet surface is fully saturated with water vapor. Consequently, a concentration gradient is established, driving a diffusive flux of vapor from the droplet surface into the free flow. In the absence of the free flow, i.e., free-flow velocity = 0 m/s, a low concentration gradient is established between the surface of the droplet and its surrounding. When the free flow is present, it brings air with lower vapor concentration, i.e., lower relative humidity, from upstream, replacing the highly concentrated air surrounding the droplet. This process increases the concentration gradient, thereby enhancing the evaporation. When the free-flow velocity is so low that the concentration gradient around the droplet remains low, even a small increase in the velocity leads to supplying the less humid air to the surrounding of the droplet and increases

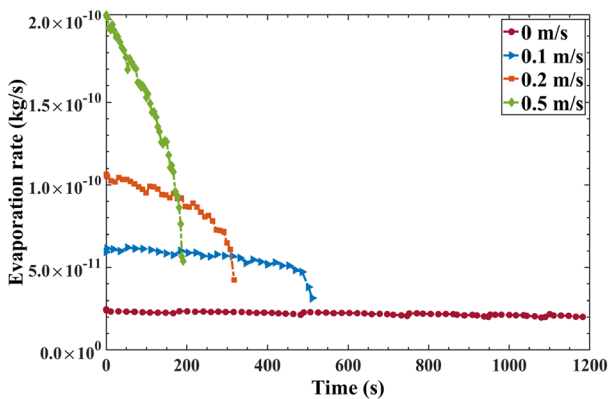
**Fig. 16** Droplet volume variation over time due to evaporation for **a** free-flow velocities in the range of 0–0.1 m/s and **b** free-flow velocities in the range of 0.5–10 m/s. **c** Impact of free-flow velocity on the droplet evaporation rate



(a)



(b)



(c)



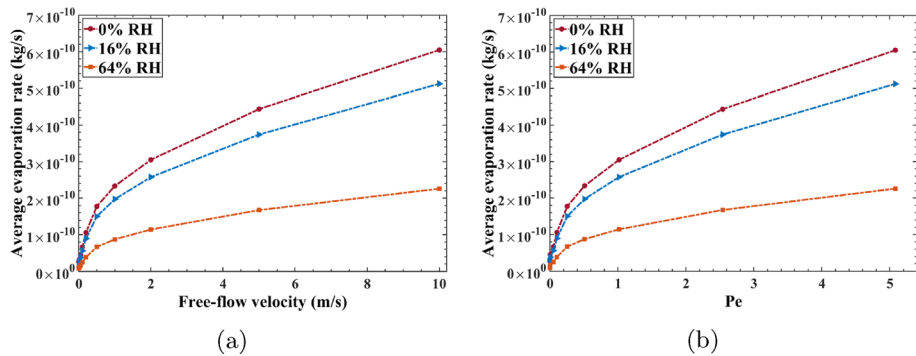


**Fig. 17** Impact of free-flow velocity on the average evaporation rate of the droplet in three free-flow relative humidities. Average evaporation rate versus **a** inlet free-flow velocity and **b** Peclet number

the evaporation rate. However, when the free-flow velocity is high enough to maintain a steep concentration gradient around the droplet, further increases in the velocity might still increase the air supply, but the resulting change in the concentration gradient, and consequently the evaporation rate, is limited. In addition, the upstream humidity determines how significant such a boosting effect is. When the upstream air contains a high vapor concentration, it affects the concentration gradient around the droplet to some extent, even in a free flow with high velocity. Consequently, increasing the free-flow velocity has a smaller influence on the evaporation rate when the air flowing into the channel has a higher relative humidity. This finding aligns with the experimental data presented Jodat and Moghiman (2012) regarding the impact of forced convection in gas flow on evaporation. It is important to note that the maximum achievable concentration gradient, through increasing free-flow velocity, is limited by the difference between the relative humidity applied at the channel inlet and the 100% relative humidity at the droplet surface.

### 3.2.6 Impact of Pore Fluid Temperature

In this section, we investigate the impact of the inlet pore body temperature on the droplet evaporation. The inlet free-flow temperature and velocity are the same for all cases and are set to 298.15 K and 5 m/s, respectively.

Figure 18a shows how the average evaporation rate changes with inlet pore body temperature. Raising the pore body temperature increases the average evaporation rate. Such an impact becomes more significant at higher temperatures. Changes in pore temperature directly influence the droplet temperature, which in turn determines the vapor pressure and vapor concentration at the droplet surface. Thus, changing the pore temperature varies the vapor concentration gradient between the droplet surface and the surrounding free flow. For instance, increasing the pore temperature increases the vapor pressure, thereby raising the vapor concentration in the air at the surface of the droplet.

The variation of the evaporation rate over time is shown in Fig. 18b for a case where the free-flow relative humidity is 16%. According to this figure, for all three humidity values, evaporation rate decreases with time, which is a result of the droplet shrinkage and less surface area available for the evaporation. Examining the graph for each humidity level reveals at least two distinct trends with different slopes. Each curve exhibits an initial

period of constant decrease in evaporation rate, followed by a change in slope leading to a steeper reduction in evaporation rate. This behavior could be related to the switch in the evaporation mode from constant contact angle to constant contact radius mode. Figure 18c shows the shrinkage of the droplet with time for different pore temperatures.

### 3.2.7 Impact of Contact Angle

To analyze the impact of the contact angle on the droplet evaporation, we examine three different contact angles. Figure 19a shows the variation of the droplet volume over time. The results indicate that a droplet on the surface with a higher contact angle evaporates more rapidly. Figure 19b shows that by increasing the contact angle, the droplet surface area also increases, which could be a reason for the faster evaporation of a droplet on a surface with a higher contact angle, as shown in Fig. 19a.

### 3.2.8 Multiple Droplets Formation and Evaporation at the Interface of a Free-Flow–Pore-Network System

We use a setup shown in Fig. 20 to show the application of the model in describing formation and evaporation of multiple droplets at the interface of a non-isothermal compositional system. In this setup, the free-flow domain is a two-dimensional channel with dimensions of  $2 \times 10^{-2} \text{ m} \times 1 \times 10^{-3} \text{ m}$  (length  $\times$  height). The porous medium is a pore network, which consists of 113 pore bodies connected by 154 pore throats. The radii of the pore bodies vary between  $4 \times 10^{-5} \text{ m}$  and  $8 \times 10^{-5} \text{ m}$ . The pore throats have radii from  $2 \times 10^{-5} \text{ m}$  to  $4 \times 10^{-5} \text{ m}$ . The free flow and the porous medium are coupled at the bottom wall of the channel. The free-flow channel is initially filled with air and the pore network is initially fully saturated with water.

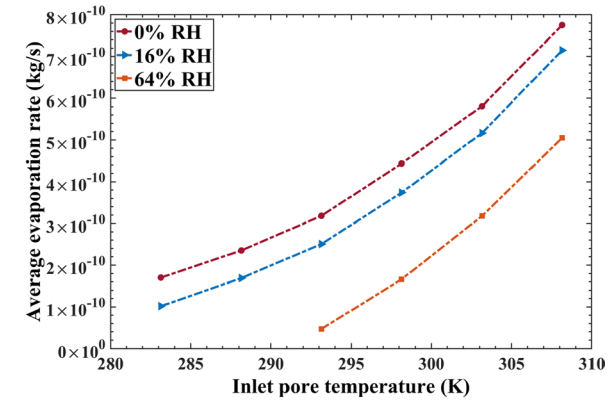
Air flows into the channel with maximum velocity of 5 m/s in a fully developed laminar profile and the temperature of 298.15 K and the outlet of the channel is exposed to atmospheric pressure. Water is injected into the inlet pores of the network with a rate of  $5 \times 10^{-7} \text{ kg/s}$  for a short time. The droplets form and grow onto pore bodies with various sizes at the interface. Then, the injection is stopped and we let the droplets evaporate. Figure 21 shows how formation and evaporation of multiple droplets affect the temperature and vapor mass fraction (concentration) distribution in the free flow.

## 4 Summary and Outlook

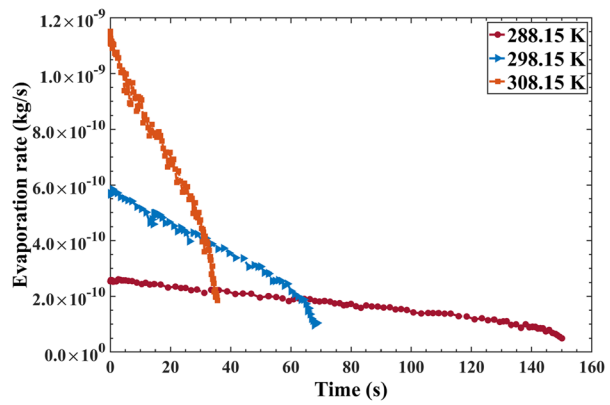
We have developed a new model to describe formation and evaporation of multiple droplets at the interface between a coupled free-flow–porous medium system. In this model, droplet evaporation into the free flow is described as a diffusion-driven phenomenon. Considering the interactions at the droplet-free-flow and droplet-pore interfaces, new coupling concepts between the free flow and the porous medium are developed, which takes storing mass, momentum and energy in the droplet as well as impact of evaporation into account.

We simulated the evaporation of a confined single droplet in a channel with different lengths and compared the results with the experimental data provided by Bansal et al. (2017). This comparison showed that our model is able to provide a proper description of the evaporation process and the impact of confinement on the evaporation rate.

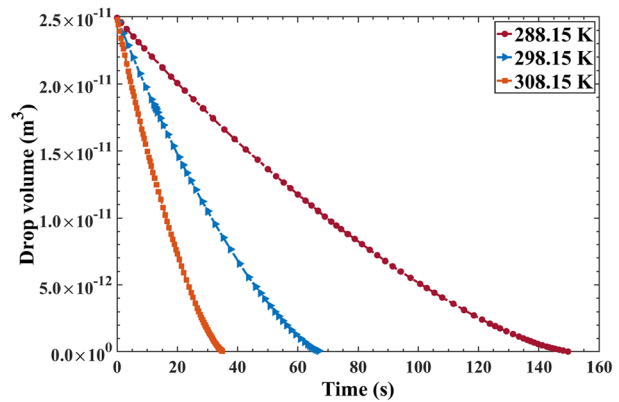
**Fig. 18** a) Variation of droplet average evaporation rate with inlet pore temperature and free-flow relative humidity, b) droplet evaporation rate over time for three pore inlet temperatures for a case where the free-flow relative humidity is 16%, and c) droplet volume variation during evaporation for three pore inlet temperatures for a case where the free-flow relative humidity is 16%



(a)



(b)



(c)

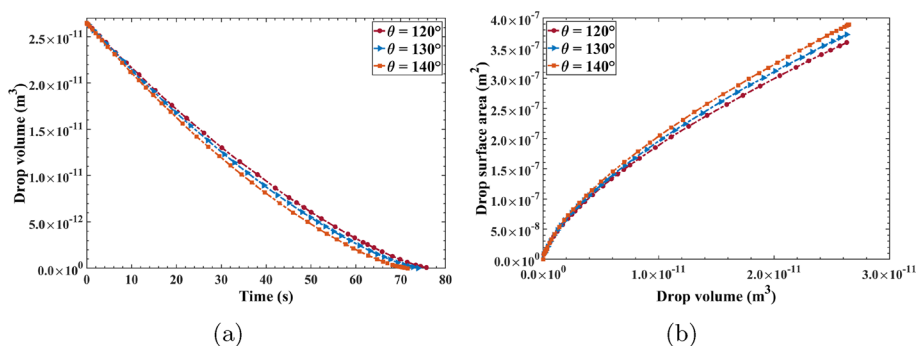


**Fig. 19** Impact of surface contact angle on a) droplet volume over time and b) droplet surface area versus droplet volume during evaporation. The inlet free-flow velocity and the inlet free-flow relative humidity, under which these analyses are conducted, are 5 m/s and 16 %, respectively. The inlet free-flow temperature and the inlet pore temperature are set to 298.15 K

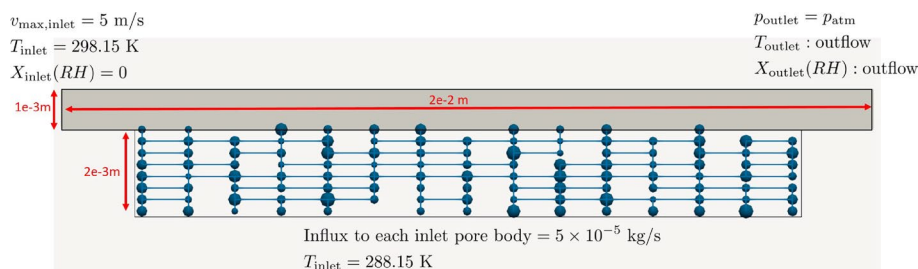


**Fig. 20** The setup used to simulate formation and evaporation of multiple droplets at the interface of a coupled free-flow-pore-network system

Furthermore, we conducted an analysis to examine how free-flow properties (e.g., free-flow velocity, relative humidity and temperature) and porous medium properties (e.g., pore size and temperature) affect the droplet evaporation. Finally, we presented an application of the new model to describe evaporation of multiple droplets at the interface. The current study provides a foundation for further developments.

In this work, we assume there is no gradient in temperature and concentration inside the droplet. However, higher change in the surface temperature of an evaporating droplet have been observed in previous studies (e.g., Hu and Larson 2002, 2005; Prakash et al. 2021). Further analysis is necessary to evaluate the influence of no-gradient assumptions made in the development of our concepts.

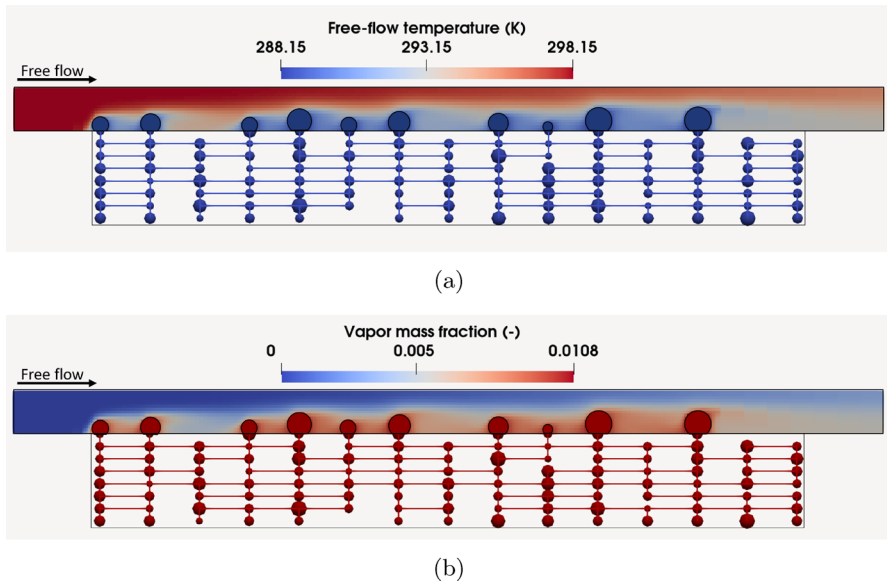


**Fig. 21** Simulation of formation and evaporation of multiple droplets at the interface: **a** impact on the temperature field and **b** impact on the vapor mass fraction

The model developed in this study provides a basis for further development and serves as a tool for other analysis of droplet evaporation, such as impact of droplet evaporation on droplet detachment and droplet evaporation in the presence of other droplets.

**Acknowledgements** We would appreciate the financial support of the Deutsche Forschungsgemeinschaft (DFG) for this project within the framework of the International Research Training Group "Droplet Interaction Technologies" (GRK 2160: DROPIT, Project Number 270852890) and the Collaborative Research Centre "Interface-Driven Multi-Field Processes in Porous Media—Flow, Transport and Deformation" (SFB 1313, Project Number 327154368).

**Author Contributions** All authors contributed to the study conception and design. Material preparation, data collection and analysis were performed by Maziar Veyskarami. The first draft of the manuscript was written by Maziar Veyskarami, and all authors commented on previous versions of the manuscript. All authors read and approved the final manuscript.

**Funding** Open Access funding enabled and organized by Projekt DEAL. This work was supported by the Deutsche Forschungsgemeinschaft (DFG, German Research Foundation) by funding the International Research Training Group "Droplet Interaction Technologies" (GRK 2160/1: DROPIT, Project Number 270852890) and the Collaborative Research Centre "Interface-Driven Multi-Field Processes in Porous Media—Flow, Transport and Deformation" (SFB 1313, Project Number 327154368).

**Data availability** All relevant data can be generated with a code which is available from the corresponding author on reasonable request.

## Declarations

**Conflict of interest** The authors have no relevant financial or non-financial interests to disclose.

**Open Access** This article is licensed under a Creative Commons Attribution 4.0 International License, which permits use, sharing, adaptation, distribution and reproduction in any medium or format, as long as you give appropriate credit to the original author(s) and the source, provide a link to the Creative Commons

licence, and indicate if changes were made. The images or other third party material in this article are included in the article's Creative Commons licence, unless indicated otherwise in a credit line to the material. If material is not included in the article's Creative Commons licence and your intended use is not permitted by statutory regulation or exceeds the permitted use, you will need to obtain permission directly from the copyright holder. To view a copy of this licence, visit <http://creativecommons.org/licenses/by/4.0/>.

## References

- Arai, M., Suidzu, T.: Porous ceramic coating for transpiration cooling of gas turbine blade. *J. Therm. Spray Technol.* **22**(5), 690–698 (2013)
- Baber, K.: *Coupling Free Flow and Flow in Porous Media in Biological and Technical Applications: From a Simple to a Complex Interface Description*. Eigenverlag des Instituts für Wasser-und Umweltsystemmodellierung, Stuttgart (2014)
- Bansal, L., Chakraborty, S., Basu, S.: Confinement-induced alterations in the evaporation dynamics of sessile droplets. *Soft Matter* **13**(5), 969–977 (2017)
- Blunt, M.J.: *Multiphase Flow in Permeable Media: A Pore-Scale Perspective*. Cambridge University Press, Cambridge (2017)
- Bormashenko, E., Musin, A., Zinigrad, M.: Evaporation of droplets on strongly and weakly pinning surfaces and dynamics of the triple line. *Colloids Surf. A* **385**(1–3), 235–240 (2011)
- Bourges-Monnier, C., Shanahan, M.: Influence of evaporation on contact angle. *Langmuir* **11**(7), 2820–2829 (1995)
- Charcosset, C.: Preparation of emulsions and particles by membrane emulsification for the food processing industry. *J. Food Eng.* **92**(3), 241–249 (2009)
- Dash, S., Garimella, S.V.: Droplet evaporation dynamics on a superhydrophobic surface with negligible hysteresis. *Langmuir* **29**(34), 10,785–10,795 (2013)
- Erbil, H.Y.: Evaporation of pure liquid sessile and spherical suspended drops: a review. *Adv. Coll. Interface Sci.* **170**(1–2), 67–86 (2012)
- Fang, X., Li, B., Petersen, E., et al.: Factors controlling the drop evaporation constant. *J. Phys. Chem. B* **109**(43), 20,554–20,557 (2005)
- Fuchs, N.A.: *Evaporation and Droplet Growth in Gaseous Media*. Pergamon, Oxford (1959)
- Glass, D.E., Dilley, A.D., Kelly, H.N.: Numerical analysis of convection/transpiration cooling. *J. Spacecr. Rocket.* **38**(1), 15–20 (2001)
- Hatte, S., Pandey, K., Pandey, K., et al.: Universal evaporation dynamics of ordered arrays of sessile droplets. *J. Fluid Mech.* **866**, 61–81 (2019)
- Hu, H., Larson, R.G.: Evaporation of a sessile droplet on a substrate. *J. Phys. Chem. B* **106**(6), 1334–1344 (2002)
- Hu, H., Larson, R.G.: Analysis of the microfluid flow in an evaporating sessile droplet. *Langmuir* **21**(9), 3963–3971 (2005)
- Jodat, A., Moghiman, M.: An experimental assessment of the evaporation correlations for natural, forced and combined convection regimes. *Proc. Inst. Mech. Eng. C J. Mech. Eng. Sci.* **226**(1), 145–153 (2012)
- Koch, T., Gläser, D., Weishaupt, K., et al.: DuMux 3-an open-source simulator for solving flow and transport problems in porous media with a focus on model coupling. *Comput. Math. Appl.* **81**, 423–443 (2021)
- Kulinich, S., Farzaneh, M.: Effect of contact angle hysteresis on water droplet evaporation from superhydrophobic surfaces. *Appl. Surf. Sci.* **255**(7), 4056–4060 (2009)
- Lubarda, V.A., Talke, K.A.: Analysis of the equilibrium droplet shape based on an ellipsoidal droplet model. *Langmuir* **27**(17), 10,705–10,713 (2011)
- Maxwell, J.C.: *Collected Scientific Papers*, vol. 2. CUP (1890)
- Orejon, D., Sefiane, K., Shanahan, M.E.: Stick-slip of evaporating droplets: substrate hydrophobicity and nanoparticle concentration. *Langmuir* **27**(21), 12,834–12,843 (2011)
- Picknett, R., Bexon, R.: The evaporation of sessile or pendant drops in still air. *J. Colloid Interface Sci.* **61**(2), 336–350 (1977)
- Prakash, J., Sikarwar, B.S., Agarwal, B.K.: Flow and thermal field in sessile droplet evaporation at various environmental conditions. *Heat Transf.* **50**(5), 4535–4551 (2021)
- Rashidi, S., Esfahani, J.A., Karimi, N.: Porous materials in building energy technologies-a review of the applications, modelling and experiments. *Renew. Sustain. Energy Rev.* **91**, 229–247 (2018)
- Schneider, M., Weishaupt, K., Gläser, D., et al.: Coupling staggered-grid and MPFA finite volume methods for free flow/porous-medium flow problems. *J. Comput. Phys.* **401**(109), 012 (2020)

- Shaikheea, A.J.D., Basu, S.: Insight into the evaporation dynamics of a pair of sessile droplets on a hydrophobic substrate. *Langmuir* **32**(5), 1309–1318 (2016)
- Shin, D.H., Lee, S.H., Jung, J.Y., et al.: Evaporating characteristics of sessile droplet on hydrophobic and hydrophilic surfaces. *Microelectron. Eng.* **86**(4–6), 1350–1353 (2009)
- Sobac, B., Brutin, D.: Triple-line behavior and wettability controlled by nanocoated substrates: influence on sessile drop evaporation. *Langmuir* **27**(24), 14,999–15,007 (2011)
- Song, H., Lee, Y., Jin, S., et al.: Prediction of sessile drop evaporation considering surface wettability. *Microelectron. Eng.* **88**(11), 3249–3255 (2011)
- Veyskarami, M., Michalkowski, C., Bringedal, C., et al.: Droplet formation, growth and detachment at the interface of a coupled free-flow-porous medium system: a new model development and comparison. *Transp. Porous Media* (2023). <https://doi.org/10.1007/s11242-023-01944-2>
- Weishaupt, K.: Model Concepts for Coupling Free Flow with Porous Medium Flow at the Pore-Network Scale: From Single-Phase Flow to Compositional Non-isothermal Two-Phase Flow. Eigenverlag des Instituts für Wasser-und Umweltsystemmodellierung, Stuttgart (2020)
- Wu, H., Veyskarami, M., Schneider, M., et al.: A new fully implicit two-phase pore-network model by utilizing regularization strategies. *Transp. Porous Media* **151**, 1–26 (2023)
- Zhu, X., Sui, P., Djilali, N.: Dynamic behaviour of liquid water emerging from a GDL pore into a PEMFC gas flow channel. *J. Power Sources* **172**(1), 287–295 (2007)

**Publisher's Note** Springer Nature remains neutral with regard to jurisdictional claims in published maps and institutional affiliations.